Photoninduced Weyl half-metal phase and spin filter effect from topological Dirac semimetals

Xiao-Shi Li[1], Chen Wang[3], Ming-Xun Deng[1],* Hou-Jian Duan[1],
Pei-Hao Fu[1], Rui-Qiang Wang[1],† L. Sheng[2], and D. Y. Xing[2]‡
[1] *Guangdong Provincial Key Laboratory of Quantum Engineering and Quantum Materials, GPETR Center for Quantum Precision Measurement, SPTE, South China Normal University, Guangzhou 510006, China*
[2] *National Laboratory of Solid State Microstructures and Department of Physics, Nanjing University, Nanjing 210093, China and*
[3] *Lab for Computational Imaging Technology and Engineering, School of Electronic Science and Engineering, Nanjing University, Nanjing 210023, China*

(Dated: February 1, 2022)

Recently discovered Dirac semimetals (DSMs) with two Dirac nodes, such as Na_3Bi and Cd_2As_3, are regarded to carry the $\mathbb{Z}_2$ topological charge in addition to the chiral charge. Here, we study the Floquet phase transition of $\mathbb{Z}_2$ topological DSMs subjected to a beam of circularly polarized light. Due to the resulting interplay of the chiral and $\mathbb{Z}_2$ charges, the Weyl nodes are not only chirality-dependent but also spin-dependent, which constrains the behaviors in creation and annihilation of the Weyl nodes in pair. Interestingly, we find a novel phase: One spinband is in Weyl semimetal phase while the other spinband is in insulator phase, and we dub it Weyl half-metal (WHM) phase. We further study the spin-dependent transport in a Dirac-Weyl semimetal junction and find a spin filter effect as a fingerprint of existence of the WHM phase. The proposed spin filter effect, based on the WHM bulk band, is highly tunable in a broad parameter regime and robust against magnetic disorder, which is expected to overcome the shortcomings of the previously proposed spin filter based on the topological edge/surface states. Our results offer a unique opportunity to explore the potential applications of topological DSMs in spintronics.

Great interest is recently triggered in spintronics towards three-dimensional (3D) topological semimetal materials[1, 2], such as Dirac semimetals (DSMs) and Weyl semimetals (WSMs). A DSM is a 3D counterpart of graphene, in which the conduction and valence bands touch, near the Fermi surface, at certain discrete Dirac point (DP). The DPs are usually unstable, because of the strong repulsion between degenerate bands[3, 4]. By breaking the time-reversal (TR) or spatial-inversion (SI) symmetry, a single DP can split into a pair of Weyl nodes, leading to the phase transition from a DSM to a WSM[5–7]. Accompanied with this, there emerge topological surface states, which are protected by the quantized Berry flux, to connect the two split Weyl nodes.

According to the classification[3], there are two distinct classes of 3D DSMs: One class is the topologically trivial DSMs possessing a single DP at a time-reversal invariant momentum and the other is the topologically nontrivial DSMs possessing a pair of DPs created by band inversion, such as Na_3Bi[2] and Cd_2As_3[8] compounds. Usually, the dispersion of the nodes is described by the momentum coupled to pseudospin while the real spin is suppressed due to spin degeneracy. Nevertheless, in topological DSMs Na_3Bi and Cd_2As_3, there is well-defined real spin and two Weyl nodes at each DP are spin-resolved. Since the Weyl nodes belong to different irreducible representations, two Weyl nodes at the same DP cannot be coupled in pair and have to seek for a partner with the same spin from the other DP. As a consequence, the two DPs including two pairs of Weyl nodes, separated by a net momentum in the Brillouin zone (BZ), are connected by two spin-polarized Fermi arcs[2, 3, 9–11]. This scenario resembles the topological insulators, carrying a non-trivial $\mathbb{Z}_2$ topological charge, and thus was named as $\mathbb{Z}_2$ topological DSMs[4, 12].

To explore the unique properties of DSMs/WSMs from transport measurements, many works[13–18] have been devoted to the longitudinal negative magnetoresistance effect due to the chiral anomaly. In addition to the chiral anomaly, the $\mathbb{Z}_2$ DSMs also carry a $\mathbb{Z}_2$ topological charge, exhibiting the $\mathbb{Z}_2$ quantum anomaly[12]. A natural question to ask in this regard is whether the existence of $\mathbb{Z}_2$ topological charge also manifests itself in any way in transport. Burkov and Kim[12] addressed that in magnetotransport, the $\mathbb{Z}_2$ topological order manifested as the spin Hall effect can lead to observable effects by narrowing the dependence of the positive magnetoconductivity on the angle between the current and the applied magnetic field, which provides a possible explanation for a recent experiment[13]. Besides, the influence of interplay between the $\mathbb{Z}_2$ and chiral anomalies on magnetoconductivity has been studied in a relativistic hydrodynamics limit[19].

Instead of the magnetotransport, the main objective of our work is to exploit the joint influence of $\mathbb{Z}_2$ topological and chiral charges on spin transport. In this Letter, we apply a beam of circularly polarized light (CPL), which is widely adopted to induce topological phase transitions of matter[20–26], to drive the phase transition of $\mathbb{Z}_2$ DSMs. We find that the CPL can create first and then annihilate the Weyl nodes in pair and finally gap them out, during which the node pairs associated with different spin

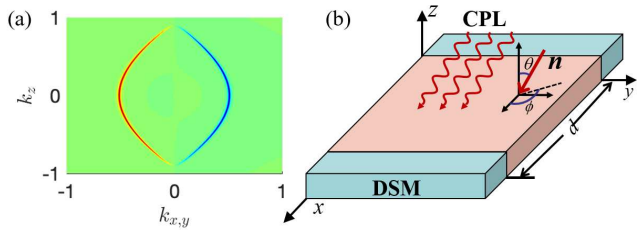

FIG. 1: (a) Spin-resolved Dirac points connected by two Fermi arcs projected on k_z-$k_{x,y}$ plane in a $\mathbb{Z}_2$ topological DSMs. The filled colors denote the magnitude of the averaged surface spin density of states $\langle\sigma_z\rangle$, with red, green and blue for $\langle\sigma_z\rangle\{>,=,<\}0$, respectively. (b) Schematic illustration of the DSM-WSM tunnel junction, in which the middle region ($0 < x < d$) is irradiated by a beam of CPL along direction $\mathbf{n} = (\sin\theta\cos\phi, \sin\theta\sin\phi, \cos\theta)$, where θ and ϕ are the polar and azimuthal angles in the spherical coordinate system.

orientations exhibit different response to the CPL. Consequently, the $\mathbb{Z}_2$ DSM can be driven into a Weyl half-metal (WHM) phase. Based on this, we further analyze the spin-dependent transport in a Dirac-Weyl semimetal junction and find that the existence of WHM phase is manifested as a fully spin-polarized current, i.e., the spin filter effect. The half-metallicity was recently employed to realize the fully spin polarized Weyl loops or the magnetic topological semimetal states[27, 28].

Floquet effective Hamiltonian- Let us start from a four-band effective Hamiltonian

$$H(\mathbf{k}) = \epsilon_0(\mathbf{k}) + M(\mathbf{k})\tau_z + v_0(k_x\sigma_z\tau_x - k_y\tau_y) + \frac{B_3 k_z}{2}(k_+^2\sigma_- + k_-^2\sigma_+)\tau_x, \quad (1)$$

with $k_\pm = k_x \pm ik_y$ and $\sigma_\pm = \sigma_x \pm i\sigma_y$, which is widely adopted to describe topological properties of $\mathbb{Z}_2$ topological DSMs Na_3Bi[9] and Cd_3As_2[10]. Here, $\sigma_{x,y,z}$ ($\tau_{x,y,z}$) are Pauli matrices for the electron spin (orbital parity or pseudospin), $\epsilon_0(\mathbf{k}) = C_0 + C_1k_z^2 + C_2(k_x^2 + k_y^2)$ and $M(\mathbf{k}) = M_0 - M_1k_z^2 - M_2(k_x^2 + k_y^2)$, with C_j, M_j, B_3, and v_0 as material parameters. If we only concentrate on the neighborhood of each gap-crossing point and neglect the high-order terms B_3, Hamiltonian (1) describes two superimposed copies of WSMs, related respectively to two spin species which is a conserved quantity. It is easy to find that, for $M_0/M_1 > 0$, there exist two DPs at $\mathbf{k}_c = (0, 0, \pm\sqrt{M_0/M_1})$, each of which contains two spin-resolved Weyl nodes. It is distinct from an ordinary DSM that the two Weyl nodes at the same DP here are nonpaired since two Weyl sectors are protected from mixing by the $\mathbb{Z}_2$ symmetry. The $\mathbb{Z}_2$ DSM structure is confirmed by the existence of two surface Fermi arcs, as shown in Fig. 1(a), connecting the two paired Weyl nodes from different DPs. The spin texture of the surface states has a helical structure, resembling the surface states of topological insulators.

When a beam of CPL irradiates along the direction $\mathbf{n} = (\sin\theta\cos\phi, \sin\theta\sin\phi, \cos\theta)$ as illustrated in Fig. 1(b), where θ and ϕ are the polar and azimuthal angles in the spherical coordinate system, the Dirac fermions can be described by a time-dependent Hamiltonian $\mathcal{H}(\mathbf{k}, t) = H(\mathbf{k} + e\mathbf{A}/\hbar)$, where

$$\mathbf{A} = A_0[\cos(\omega t)\mathbf{e}_1 - \eta\sin(\omega t)\mathbf{e}_2] \quad (2)$$

is vector potential for the CPL with amplitude A_0, frequency ω and $\eta = \pm 1$ for right/left polarization. The spacial dependence of A_0 can be neglected, as we consider that the light wavelength is much larger than the device[29]. Here, $\mathbf{e}_1 = (\cos\theta\cos\phi, \cos\theta\sin\phi, -\sin\theta)$ and $\mathbf{e}_2 = (\sin\phi, -\cos\phi, 0)$, satisfying $\mathbf{e}_1 \cdot \mathbf{e}_2 = 0$, are two unit vectors perpendicular to the incident direction of the light. Employing the Floquet theorem[20–26] and focusing ourselves on the off-resonant regime, in which $\hbar\omega$ is greater than the width of the static energy band, we derive an effective Hamiltanion[29]

$$\mathcal{H}_{\rm eff}(\mathbf{k}) = \tilde{\epsilon}_0(\mathbf{k}) + \tilde{M}(\mathbf{k})\tau_z + v_0(k_x\sigma_z\tau_x - k_y\tau_y) - \lambda\sigma_z\tau_z + v_1k_z(\cos\phi\tau_x - \sin\phi\sigma_z\tau_y) - v_2(k_x\tau_x - k_y\sigma_z\tau_y), \quad (3)$$

where B_3 is dropped due to smallness, and denote $\lambda = \eta\frac{v_0^2k_A^2\cos\theta}{\omega}$, $v_1 = \eta\frac{2M_1k_A^2\sin\theta}{\omega}v_0$, and $v_2 = \eta\frac{2M_2k_A^2\cos\theta}{\omega}v_0$, with $k_A = eA_0/\hbar$ characterizing the CPL intensity. The renormalized parameters in the first two terms are given by $\tilde{\epsilon}_0(\mathbf{k}) = \epsilon_0(\mathbf{k})|_{C_0\to C_0+C_0'}$ and $\tilde{M}(\mathbf{k}) = M(\mathbf{k})|_{M_0\to M_0-M_0'}$, where $C_0' = k_A^2(\frac{1+\eta^2}{2}C_2 + C_-\sin^2\theta)$ and $M_0' = k_A^2(\frac{1+\eta^2}{2}M_2 + M_-\sin^2\theta)$, with $C_- = (C_1 - C_2)/2$ and $M_- = (M_1 - M_2)/2$.

CPL-driven WHM phase- As it shows, in the presence of the CPL, the TR symmetry is broken explicitly, such that the DPs are expected to split into two pairs of spin-resolved Weyl nodes. The quasienergy spectrum of the effective Hamiltonian (3) is

$$\epsilon_{s,\pm}(\mathbf{k}) = \tilde{\epsilon}_0(\mathbf{k}) \pm \sqrt{|\tilde{M}_s(\mathbf{k})|^2 + v_s^2(\tilde{k}_{x,s}^2 + \tilde{k}_{y,s}^2)}, \quad (4)$$

where $\tilde{k}_{x,s} = k_x + s\frac{v_1}{v_s}k_z\cos\phi$ and $\tilde{k}_{y,s} = k_y + s\frac{v_1}{v_s}k_z\sin\phi$, with $v_s = v_0 - sv_2$ and $\tilde{M}_s(\mathbf{k}) = \tilde{M}(\mathbf{k}) - s\lambda$. In contrast to the static spectrum of Hamiltonian (1), the CPL-driven spectrum becomes spin-dependent. The evolution of the spin-resolved quasienergy spectrum with the CPL intensity is plotted in Fig. 2(a). There are four Weyl nodes located at

$$\mathbf{k}_{c,\pm}^s = \pm(sv_1\cos\phi, sv_1\sin\phi, -v_s)k_{w,s}/v_s \quad (5)$$

with $k_{w,s} = \sqrt{\frac{M_0 - (M_0' + s\lambda)}{M_1 + v_1^2M_2/v_s^2}}$, which correspond to the vertexes of the dispersion. In the presence of the CPL, the two Weyl nodes overlapping at one DP are separated and, simultaneously, the Berry curvature emerges in the whole momentum space, starting from a Weyl node

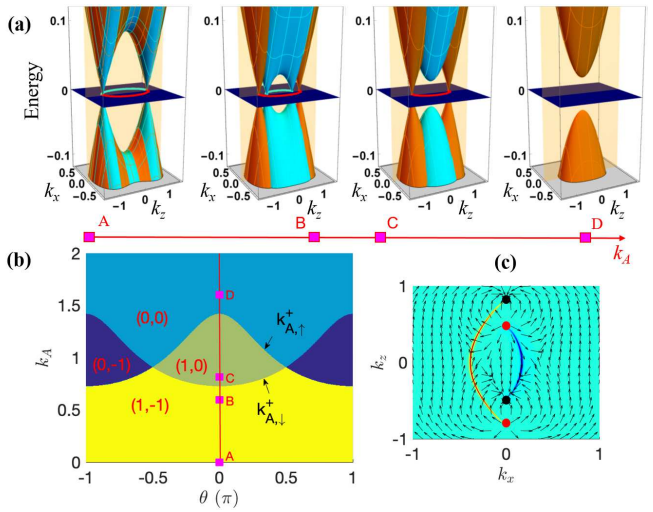

FIG. 2: (a) Evolution of the spin-resolved quasienergy spectrum with the CPL intensity $k_A = (0, 0.6, 0.8, 1.6) \times \mathrm{nm}^{-1}$ from left to the right side, which correspond to points A-D marked in (b). The other CPL parameters are $\hbar\omega = 1.0$ eV[30, 31], $\phi = 0$ and $\theta = 0$. The brown and blue regions represent the spin-↑ and spin-↓ Weyl sectors, respectively, and the lines connecting the nodes denote the surface Fermi arcs. (b) The phase diagram characterized with the spin-dependent Chern fluxes $(C_\uparrow, C_\downarrow)$ in the k_A-θ parameter space, and (c) the Berry curvature distribution corresponding to point B, where the red and black filled circles stand for the Weyl nodes with a positive and negative chiral charge, respectively. The calculation is carried out for Na_3Bi, whose parameters can be found in Ref. [9].

with positive chiral charge and ending at one with negative chiral charge [seeing Fig. 2(c)]. Notice that the split Weyl nodes are not only chirality-dependent but also spin-dependent, as shown in Fig. 2(a), where the brown and blue regions represent the spin-↑ and spin-↓, respectively, and two nodes with the same spin are connected by an open Fermi arc. Importantly, with increase of k_A, the distance $2k_{w,s}$ between the paired Weyl nodes would reduce because of the CPL-renormalized term M_0'. Consequently, in certain crucial value, the paired Weyl nodes with opposite chirality can be merged in momentum space and then gapped out. Notice that the different spin species have different critical values, which originate from the renormalized spin-dependent Dirac mass term $s\lambda$. It is interesting to find a phase as illustrated by the third diagram of Fig. 2(a), where the spin-↑ species still remains at the WSM phase but the spin-↓ species enters the insulator phase, which exhibits a typical characteristic of well-known spin half-metals. This novel Weyl phase has not been reported before and we dub it Weyl half-metal (WHM) phase. As k_A further increases, both pairs of the Wely nodes could be gapped out, and finally the system undergoes a transition to an insulating phase, as shown in the last diagram of Fig. 2(a).

In order to identify these different topological phases, we can further classify them according to the spin-dependent Chern fluxes $(C_\uparrow, C_\downarrow)$ at the $k_z = 0$ BZ cross section[3]. With the Berry curvature[4] $\Omega_{s,ij}(\mathbf{k}) = \frac{1}{2|d_s|^3}\epsilon_{abc} d_{s,a}\partial_i d_{s,b}\partial_j d_{s,c}$, where ϵ_{abc} denotes the antisymmetric tensor and $d_s = \left(sv_0\tilde{k}_{x,s}, v_0\tilde{k}_{y,s}, \tilde{M}_s(\mathbf{k})\right)$, we find

$$C_s = -\frac{s}{2}[\mathrm{sgn}(M_2) + \mathrm{sgn}(M_0 - M_0' - s\lambda)] \qquad (6)$$

for s spin component. In Fig. 2(b), we plot the phase diagram in the k_A-θ parameter space. From the bottom to the top, e.g., points A to D, the phase is in order DSM phase ($k_A = 0$), WSM phase $(1, -1)$, WHM phase $(1, 0)$ or $(0, -1)$, and normal insulating phase $(0, 0)$, whose dispersions are depicted in Fig. 2(a), respectively. The phase boundaries are determined by the equation $M_2 + M_- \sin^2\theta + s\eta v_0^2 \cos\theta/\omega = M_0/k_A^2$ via $k_{w,s} = 0$. Subsequently, we can derive the crucial values for the light intensity to be

$$k_{A,s}^{\eta} = \sqrt{\frac{M_0}{M_2 + M_- \sin^2\theta + s\eta v_0^2\cos\theta/\omega}}. \qquad (7)$$

The WHM phase emerges in the range of $(k_{A,\downarrow}^+, k_{A,\uparrow}^+)$ for $|\theta| < \frac{\pi}{2}$, where only the spin-↑ WHM phase exists. The spin-↓ WHM phase can be realized just by reversing the polarization η of the CPL or by tuning the incident direction $|\theta| > \frac{\pi}{2}$ to be in the WHM region $(0, -1)$. If $k_A > k_{A,\uparrow}^+$, the CPL-driven DSM would cross over to a normal insulator with spin-dependent Chern fluxes $(0, 0)$, where both pairs of the Weyl nodes are gapped out. Also, we can tune the thresholds $k_{A,\downarrow}^+$ and $k_{A,\uparrow}^+$ by changing the incident direction of the CPL due to the rotation of the Weyl nodes in the k_x-k_z plane. For a specific value $\theta = \pm\pi/2$, the thresholds $k_{A,\downarrow}^+ = k_{A,\uparrow}^+$ and thus the WHM phase region vanishes.

CPL-modulated spin-dependent transmission- In the following, we study the transport fingerprint related to the WHM phase. We construct a DSM/WSM sandwich junction, as shown in Fig. 1(b), where the middle WSM region $0 < x < d$ is formed due to the irradiation by a beam of CPL. The eigenequation for the DSM reservoirs can be obtained as

$$[E - \epsilon_0(\mathbf{k})]^2 = [M(\mathbf{k})]^2 + v_0^2(k_x^2 + k_y^2), \qquad (8)$$

from which we can determine k_x for fixed k_y, k_z and the Fermi energy $E = E_\mathrm{F}$. We are interested in the electron transport near the gap-closing points, and so the unimportant terms $\epsilon_0(\mathbf{k})$ and $M_2(k_x^2 + k_y^2)$ can be neglected. It is easy to find the wavefuncitons in different regions. By matching the wavefunctions at the interfaces $\psi_s(x = 0^-) = \psi_s(x = 0^+)$ and $\psi_s(x = d^-) = \psi_s(x = d^+)$, we can obtain the transmission coefficient as

$$t_s = \frac{2\mathcal{F}_1\mathcal{F}_2 e^{-i(k_1 + s\frac{v_1}{v_s}k_z\cos\phi)d}}{2\mathcal{F}_1\mathcal{F}_2\cos(k_2 d) - i(\mathcal{F}_1^2 + \mathcal{F}_2^2 + \Delta_y^2)\sin(k_2 d)}, \qquad (9)$$

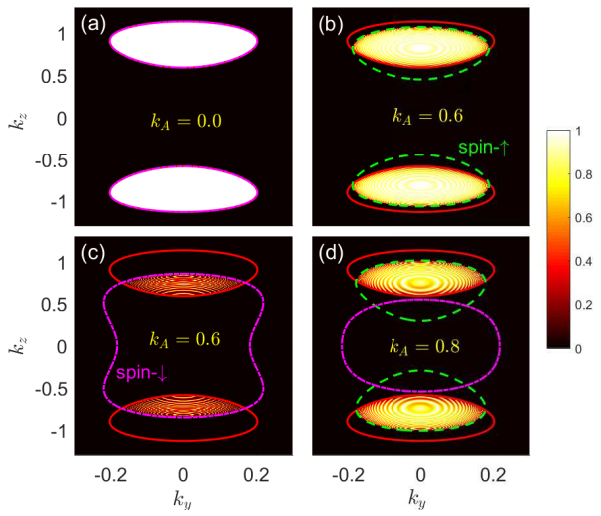

FIG. 3: Distribution of the spin-dependent transmission probability $T_\uparrow(k_y, k_z)$ and $T_\downarrow(k_y, k_z)$ on the k_y-k_z plane, with (a) for $k_A = 0$ where $T_\uparrow(k_y, k_z)$ coincides with $T_\downarrow(k_y, k_z)$ completely, (b)-(c) for $k_A = 0.6$, and (d) for $k_A = 0.8$ where $T_\downarrow(k_y, k_z) = 0$. The lines represent the projections of the Fermi surfaces, with red-solid, green-dash and pink-dash-dot for the reservoirs, the spin-↑ and spin-↓ components in the middle WSM region, respectively. Here, $E_F = 0.05$ eV, $d = 400$nm, $\phi = \pi/2$, and other parameters are the same as Fig. 2(a).

where k_1 represents the positive root of Eq. (8) and k_2 can be obtained similarly from the eigenequation of the CPL-driven region. In Eq. (9), $\mathcal{F}_1 = v_0 k_1[E - \tilde{M}_s(\mathbf{k})]$, $\mathcal{F}_2 = v_s k_2[E - M(\mathbf{k})]$ and

$$\Delta_y = v_0 k_y[E - \tilde{M}_s(\mathbf{k})] - v_s \tilde{k}_{y,s}[E - M(\mathbf{k})]. \quad (10)$$

The spin-dependent transmission probability can be obtained by $T_s(k_y, k_z) = |t_s|^2$. For $d \gg 1$, the transmission probability is finite only when $k_{1,2} \in$ real, i.e., k_y and k_z are within the overlapping region of the projected Fermi surfaces of the reservoirs and the CPL-driven WSM.

The distributions of the spin-dependent transmission probability $T_\uparrow(k_y, k_z)$ and $T_\downarrow(k_y, k_z)$ on the k_y-k_z plane are plotted in Fig. 3. In the absence of the CPL, $T_\uparrow(k_y, k_z) = T_\downarrow(k_y, k_z) = 1$ for all the incident electron states, as shown in Fig. 3(a), because of the perfect matching of the Fermi surfaces between different regions. With introduction of the CPL, the Weyl nodes are split and move in the k_z axis, which leads to mismatch of wave vectors between the middle region and the reservoirs[32, 33]. Due to the broken TR symmetry, two spin species exhibit different splitting distances along k_z and so different shapes of the Fermi surfaces in Figs. 3(b) and (c). Consequently, the spin-↑ Fermi surface in the middle WSM region has a larger overlapping with that in the DSM reservoirs (denoted by the red solid lines) whereas the spin-↓ Fermi surface has smaller

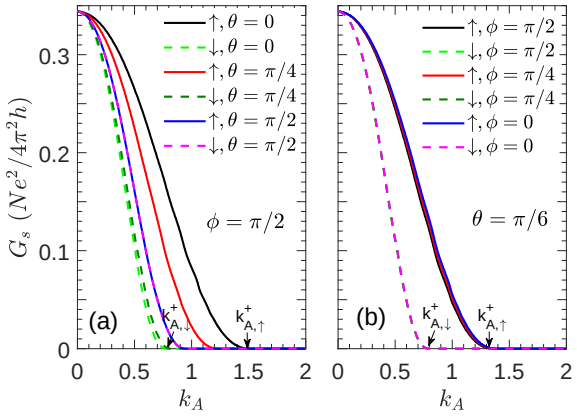

FIG. 4: Spin-dependent conductances $G_\uparrow$ and $G_\downarrow$ as a function of the CPL intensity k_A for (a) different θ with $\phi = \pi/2$ and for (b) different ϕ with $\theta = \pi/6$. Other parameters are the same as in Fig. 3.

overlapping. Naturally, there emerges interesting spin-dependent electron transport processes. With further increase of irradiation intensity k_A, the spin-↓ Fermi surfaces in the middle region would disconnect from that of the reservoirs and so has no contribution to the electron transport, as shown in Fig. 3(d). In this situation, there will emerge a fully spin-polarized current, implying that the irradiated region has entered the WHM phase $(1, 0)$.

Fully spin-polarized conductance- The spin-dependent conductance can be calculated by the Landauer formula

$$G_s = \frac{e^2}{h} \sum_{k_y, k_z} T_s(k_y, k_z), \quad (11)$$

where the summation runs over all the incident modes at the Fermi surface, i.e., the k_y-k_z surface BZ. In Fig. 4(a), we plot the spin-dependent conductance $G_\uparrow$ and $G_\downarrow$ as a function of the CPL intensity k_A for different polar angles θ. As k_A increases, the spin-dependent conductances $G_\uparrow$ and $G_\downarrow$ will decrease due to suppression of the transmission probability, and after certain thresholds they vanish completely. Although both conductances reduce with k_A, $G_\downarrow$ decays with a faster rate than $G_\uparrow$, such that the threshold $k^+_{A,\downarrow}$ for spin-↓ current is lower than $k^+_{A,\uparrow}$ for spin-↑ current. For $k_A \in (k^+_{A,\downarrow}, k^+_{A,\uparrow})$, the electric current is spin-↑ fully-polarized, exhibiting a perfect spin filter effect. The spin filter region $(k^+_{A,\downarrow}, k^+_{A,\uparrow})$ is quite sensitive to the incident direction θ of the CPL. As the polar angle deviates from $\theta = 0$, the spin filter region $(k^+_{A,\downarrow}, k^+_{A,\uparrow})$, as shown in Fig. 4(a), will reduce. For a specific value $\theta = \pi/2$, there is no spin-polarized conductance because the WHM phase does not exits in this situation, as seen in Fig. 2(b). In contrast, the spin filter region, as shown in Fig. 4(b), is almost independent on the azimuthal angle ϕ of the CPL, since the thresholds given by Eq. (7) is irrelevant with ϕ.

Conclusion and remarks- We have theoretically studied the Floquet phase transition of $\mathbb{Z}_2$ topological DSMs subjected to a beam of CPL. Due to the interplay of the chiral and $\mathbb{Z}_2$ charges, the Weyl nodes are not only chirality-dependent but also spin-dependent, which constrains the behaviors in creation and annihilation of the Weyl nodes in pair. During the evolution of Weyl nodes with the CPL intensity, we find an entirely new WHM phase: One spinband is in WSM phase while the other spinband is in insulator phase, which simultaneously possesses the characteristic of both WSMs and half-metals. This novel phase has not been reported before. We have also checked that an applied magnetic field/magnetic perturbation or a linearly polarized light can not achieve this WHM phase, because they cannot realize the creation and annihilation of the Weyl nodes pair at the same time[29].

We further study the spin-dependent transport and find a spin filter effect as a fingerprint of existence of the WHM phase. Indeed, spin filter transistor is an important device in spintronics, with numerous works focus on its implementation using the topological edge/surface states[34–38]. However, these have several typical shortcomings: (1) Disturbance from unpolarized bulk band; (2) Easily suffering from magnetic disorder; (3) Only appearing at several specific energy position, which is difficult to manipulate experimentally. Recently, Tasi *et.al.*[39] proposed a silicene-based spin filter device to reduce above shortcomings by taking advantage of the bulk carriers. Here, we propose the spin filter effect based on the WHM bulk band, which is highly tunable in a broad parameter regime and robust against magnetic disorder. Moreover, we can implement it, no needing other additional conditions in contrast to previous works.

In realistic experiments, one can realize our proposed model using a beam of gaussian profile light or replacing Weyl-semimetal reservoirs with normal-metal electrodes, as discussed in supplementary material[29]. The threshold of the incident radiation intensity for the system entering the WHM phase is determined by Eq.(7). For Na_3Bi[9], with $k_A = eA_0/\hbar$ and $A_0 = E_0/\omega$, we estimate the threshold of the irradiated electric field to be $E_0 \simeq 7.2 \times 10^8 V/m$ for $\hbar\omega = 1$ eV. For Cd_3As_2[**?**], the threshold can be reduced by an order in magnitude $E_0 \simeq 5 \times 10^7 V/m$ for $\hbar\omega = 0.5$eV. These radiation intensities are within the current experimental accessibility[40, 41]. In the normal metal/Weyl semimetal/normal metal junction, more lower critical radiation intensity can be achieved.

This work was supported by the National Natural Science Foundation of China under Grants No. 11874016, 11904107, the Key Program for Guangdong NSF of China under Grant No. 2017B030311003, GDUPS(2017), the State Key Program for Basic Researches of China under Grants No. 2015CB921202 (L. S.) and No. 2017YFA0303203 (D. Y. X.), and by the Innovation Project of Graduate School of South China Normal University.

Xiao-Shi Li and Chen Wang contributed equally to this work.

* Electronic address: dengmingxun@scnu.edu.cn
† Electronic address: wangruiqiang@m.scnu.edu.cn
‡ Electronic address: dyxing@nju.edu.cn

[1] N. P. Armitage, E. J. Mele, and A. Vishwanath, Rev. Mod. Phys. **90**, 015001 (2018).
[2] Z. K. Liu, B. Zhou, Y. Zhang, Z. J. Wang, H. M. Weng, D. Prabhakaran, S.-K. Mo, Z. X. Shen, Z. Fang, X. Dai, Z. Hussain, and Y. L. Chen, Science **343**, 864 (2014).
[3] B.-J. Yang and N. Nagaosa, Nat. Commun. **5**, 4898 (2014).
[4] E. V. Gorbar, V. A. Miransky, I. A. Shovkovy, and P. O. Sukhachov, Phys. Rev. B **91**, 121101 (2015).
[5] S. Raza, A. Sirota, and J. C. Y. Teo, Phys. Rev. X **9**, 011039 (2019).
[6] S. Han, G. Y. Cho, and E.-G. Moon, Phys. Rev. B **98**, 085149 (2018).
[7] M.-X. Deng, W. Luo, R.-Q. Wang, L. Sheng, and D. Y. Xing, Phys. Rev. B **96**, 155141 (2017).
[8] M. Neupane, S.-Y. Xu, R. Sankar, N. Alidoust, G. Bian, C. Liu, I. Belopolski, T.-R. Chang, H.-T. Jeng, H. Lin, A. Bansil, F. Chou, and M. Z. Hasan, Nat. Commun. **5**, 3786 (2014).
[9] Z. Wang, Y. Sun, X.-Q. Chen, C. Franchini, G. Xu, H. Weng, X. Dai, and Z. Fang, Phys. Rev. B **85**, 195320 (2012).
[10] Z. Wang, H. Weng, Q. Wu, X. Dai, and Z. Fang, Phys. Rev. B **88**, 125427 (2013).
[11] X. Wan, A. M. Turner, A. Vishwanath, and S. Y. Savrasov, Phys. Rev. B **83**, 205101 (2011).
[12] A. A. Burkov and Y. B. Kim, Phys. Rev. Lett. **117**, 136602 (2016).
[13] J. Xiong, S. K. Kushwaha, T. Liang, J. W. Krizan, M. Hirschberger, W. Wang, R. J. Cava, and N. P. Ong, Science **350**, 413 (2015).
[14] C.-Z. Li, L.-X. Wang, H. Liu, J. Wang, Z.-M. Liao, and D.-P. Yu, Nat. Commun. **6**, 10137 (2015).
[15] C. Zhang, E. Zhang, W. Wang, Y. Liu, Z.-G. Chen, S. Lu, S. Liang, J. Cao, X. Yuan, L. Tang, Q. Li, C. Zhou, T. Gu, Y. Wu, J. Zou, and F. Xiu, Nat. Commun. **8**, 13741 (2017).
[16] X. Huang, L. Zhao, Y. Long, P. Wang, D. Chen, Z. Yang, H. Liang, M. Xue, H. Weng, Z. Fang, X. Dai, and G. Chen, Phys. Rev. X **5**, 031023 (2015).
[17] M.-X. Deng, G. Y. Qi, R. Ma, R. Shen, R.-Q. Wang, L. Sheng, and D. Y. Xing, Phys. Rev. Lett. **122**, 036601 (2019).
[18] S. Liang, J. Lin, S. Kushwaha, J. Xing, N. Ni, R. J. Cava, and N. P. Ong, Phys. Rev. X **8**, 031002 (2018).
[19] M. Rogatko and K. Wysokinski, J. High Energ. Phys. **2018**, 136 (2018).
[20] M. S. Rudner, N. H. Lindner, E. Berg, and M. Levin, Phys. Rev. X **3**, 031005 (2013).
[21] P. Titum, N. H. Lindner, M. C. Rechtsman, and G. Refael, Phys. Rev. Lett. **114**, 056801 (2015).
[22] A. Farrell and T. Pereg-Barnea, Phys. Rev. Lett. **115**,

106403 (2015).
[23] C.-K. Chan, P. A. Lee, K. S. Burch, J. H. Han, and Y. Ran, Phys. Rev. Lett. **116**, 026805 (2016).
[24] Z. Yan and Z. Wang, Phys. Rev. Lett. **117**, 087402 (2016).
[25] M.-X. Deng, W. Y. Deng, D. X. Shao, R.-Q. Wang, R. Shen, L. Sheng, and D. Y. Xing, Phys. Rev. B **95**, 115102 (2017).
[26] P.-H. Fu, H.-J. Duan, R.-Q. Wang, and H. Chen, Physics Letters A **381**, 3499 (2017).
[27] G. Chang, S.-Y. Xu, H. Zheng, B. Singh, C.-H. Hsu, G. Bian, N. Alidoust, I. Belopolski, D. S. Sanchez, S. Zhang, H. Lin, and M. Z. Hasan, Scientific Reports **6**, 38839 (2016).
[28] C. Chen, Z.-M. Yu, S. Li, Z. Chen, X.-L. Sheng, and S. A. Yang, Phys. Rev. B **99**, 075131 (2019).
[29] See the Supplemental Material for a detail derivation of Eq. (3) of the main text and discussion on the dependence of the transmission probability and conductances on d, the role of an applied magnetic field/magnetic perturbation or a linearly polarized light, and two setups to overcome the light confinement in experiments.
[30] M. A. Sentef, M. Claassen, A. F. Kemper, B. Moritz, T. Oka, J. K. Freericks, and T. P. Devereaux, Nat. Commun. **6**, 7047 (2015).
[31] E. J. Sie, *Coherent Light-Matter Interactions in Monolayer Transition-Metal Dichalcogenides, Springer Theses* (Springer, Berlin, 2018).
[32] N. Stander, B. Huard, and D. Goldhaber-Gordon, Phys. Rev. Lett. **102**, 026807 (2009).
[33] A. F. Young and P. Kim, Nat. Phys. **5**, 222 (2009).
[34] A. Rycerz, J. Tworzydło, and C. W. J. Beenakker, Nat. Phys. **3**, 172 (2007).
[35] C. Brüne, A. Roth, H. Buhmann, E. M. Hankiewicz, L. W. Molenkamp, J. Maciejko, X.-L. Qi, and S.-C. Zhang, Nat. Phys. **8**, 485 (2012).
[36] R.-Q. Wang, L. Sheng, R. Shen, B. Wang, and D. Y. Xing, Phys. Rev. Lett. **105**, 057202 (2010).
[37] S. Rachel and M. Ezawa, Phys. Rev. B **89**, 195303 (2014).
[38] S. Zamani and R. Farghadan, Phys. Rev. Applied **10**, 034059 (2018).
[39] W.-F. Tsai, C.-Y. Huang, T.-R. Chang, H. Lin, H.-T. Jeng, and A. Bansil, Nat. Commun. **4**, 1500 (2013).
[40] Y. H. Wang, H. Steinberg, P. Jarillo-Herrero, and N. Gedik, Science **342**, 453 (2013).
[41] F. Mahmood, C.-K. Chan, Z. Alpichshev, D. Gardner, Y. Lee, P. A. Lee, and N. Gedik, Nat. Phys. **12**, 306 (2016).

Supplementary material A: Derivation for the effective Hamiltonian Eq. (3)

In this appendix, we provide the details for derivation of Eq. (3) in the main text.

The Dirac fermions driven by a beam of circularly polarized light (CPL) can be described by a time-dependent Hamiltonian $\mathcal{H}(\mathbf{k},t) = H(\mathbf{k}+e\mathbf{A}/\hbar)$, where the vector potential $\mathbf{A}$ is given by Eq. (2) of the main text. According to Ref. [9] of the main text, we give out the system parameters of Na_3Bi for convenience as follows: $v_0 = 2.4598\ eV\mathring{A}$, $C_0 = -0.06382\ eV$, $C_1 = 8.7536\ eV\mathring{A}^2$, $C_2 = -8.4008\ eV\mathring{A}^2$, $M_0 = -0.08686\ eV$, $M_1 = -10.6424\ eV\mathring{A}^2$ and $M_2 = -10.3610\ eV\mathring{A}^2$. Employing the Floquet theorem[1–5], one can expand $\mathcal{H}(\mathbf{k},t)$ in the Floquet basis as

$$\mathcal{H}_{n,n'} = n\omega\delta_{n,n'} + \frac{1}{T}\int_0^T dt e^{i(n-n')\omega t}\mathcal{H}(\mathbf{k},t)\,, \tag{A1}$$

where $T = 2\pi/\omega$ is the period of the CPL. By diagonalizing the Floquet Hamiltonian $\mathcal{H}$, it is easy to obtain the Floquet states and the quasienergy spectrum. The Floquet states, in fact, are uniquely and completely parametrized by quasienergies in the "first quasienergy Brillouin zone" $-\hbar\omega/2 \leqslant \epsilon < \hbar\omega/2$, where ϵ denotes the quasienergy.

The retarded Green's function is defined as $G^r(\epsilon) = \frac{1}{\epsilon+i0^+-\mathcal{H}}$, from which one can express the Floquet retarded Green's function for the n-th Floquet band as[6]

$$G^r_{n,n}(\epsilon) = \frac{1}{\epsilon^+ - \mathcal{H}_{n,n} - \sum_{m\neq n}\mathcal{H}_{n,m}G^r_{m,m}(\epsilon)\mathcal{H}_{m,n}}\,, \tag{A2}$$

where we have adopted abbreviation $\epsilon^+ = \epsilon + i0^+$. By inspecting the poles of the retarded Green's function, we can obtain an effective Hamiltonian for the n-th Floquet band

$$\mathcal{H}_{\mathrm{eff},n}(\mathbf{k}) = \mathcal{H}_{n,n} + \sum_{m\neq n}\mathcal{H}_{n,m}G^r_{m,m}(\epsilon)\mathcal{H}_{m,n}\,. \tag{A3}$$

For a relatively weak radiation field, the properties of the CPL-driven DSM are dominated by the $|n=0\rangle$ Floquet state, such that we would focus ourselves on the behavior of this Floquet state. In the limit of off-resonant approximation, i.e., high-frequency light with $\hbar\omega$ greater than the width of the static energy band, real photon-absorption processes are suppressed. In this case, we can safely approximate $G^r_{n,n}(\epsilon) \simeq -\frac{1}{n\omega} + O(\frac{1}{\omega^2})$ for $n \neq 0$. As a consequence, for the $|n=0\rangle$ Floquet state, $\mathcal{H}_{\mathrm{eff},n}(\mathbf{k})$ can be closed as

$$\mathcal{H}_{\mathrm{eff}}(\mathbf{k}) = \mathcal{H}_{n,n}\delta_{n,0} + \sum_{m>0}\frac{1}{m\omega}[\mathcal{H}_{m,0},\mathcal{H}_{0,m}] + O(\frac{1}{\omega^2})\,, \tag{A4}$$

where we noted $\mathcal{H}_{\mathrm{eff}}(\mathbf{k}) \equiv \mathcal{H}_{\mathrm{eff},0}(\mathbf{k})$ for brevity. As can be seen, Eq. (A4) exactly recovers the result given in Ref. [5].

By using Hamiltonian (1) and Eq. (2) of the main text, it is easy to verify $[\mathcal{H}_{n,0},\mathcal{H}_{0,n}] = 0$ for $n \geqslant 2$. If neglecting the higher-order terms tied to B_3, we find $[\sigma_z, H(\mathbf{k})] = 0$ and the Hamiltonian can be separated into two 2×2 blocks, which can be labelled by the eigenvalues of σ_z, $s = \pm 1$. Subsequently, we obtain

$$\begin{aligned}
\mathcal{H}^s_{0,0} &= \epsilon_0(\mathbf{k}) + k_A^2(\frac{1+\eta^2}{2}C_2 + \frac{C_1-C_2}{2}\sin^2\theta) + V_0\begin{pmatrix}1&0\\0&-1\end{pmatrix}\,,\\
\mathcal{H}^s_{1,0} &= \frac{v_0k_A}{2}\begin{pmatrix}0 & e^{is\phi}(s\cos\theta-\eta)\\ e^{-is\phi}(s\cos\theta+\eta) & 0\end{pmatrix} + V_1\begin{pmatrix}1&0\\0&-1\end{pmatrix}\,,\\
\mathcal{H}^s_{0,1} &= \frac{v_0k_A}{2}\begin{pmatrix}0 & e^{is\phi}(s\cos\theta+\eta)\\ e^{-is\phi}(s\cos\theta-\eta) & 0\end{pmatrix} + V_{-1}\begin{pmatrix}1&0\\0&-1\end{pmatrix}\,,
\end{aligned} \tag{A5}$$

with

$$\begin{aligned}
V_0 &= M(\mathbf{k}) - k_A^2(\frac{1+\eta^2}{2}M_2 + \frac{M_1-M_2}{2}\sin^2\theta)\,,\\
V_1 &= k_A[M_1k_z\sin\theta - M_2k_x(\cos\theta\cos\phi - i\eta\sin\phi) - M_2k_y(\cos\theta\sin\phi + i\eta\cos\phi)]\,,\\
V_{-1} &= k_A[M_1k_z\sin\theta - M_2k_x(\cos\theta\cos\phi + i\eta\sin\phi) - M_2k_y(\cos\theta\sin\phi - i\eta\cos\phi)]\,.
\end{aligned} \tag{A6}$$

From the above equations, we can further derive

$$[\mathcal{H}^s_{1,0},\mathcal{H}^s_{0,1}] = 2\eta v_0M_1k_A^2\sin\theta\begin{pmatrix}0 & k_ze^{is\phi}\\ k_ze^{-is\phi} & 0\end{pmatrix} - 2\eta v_0M_2k_A^2\cos\theta\begin{pmatrix}0 & k_x+isk_y\\ k_x-isk_y & 0\end{pmatrix} - s\eta v_0^2k_A^2\cos\theta\begin{pmatrix}1&0\\0&-1\end{pmatrix}. \tag{A7}$$

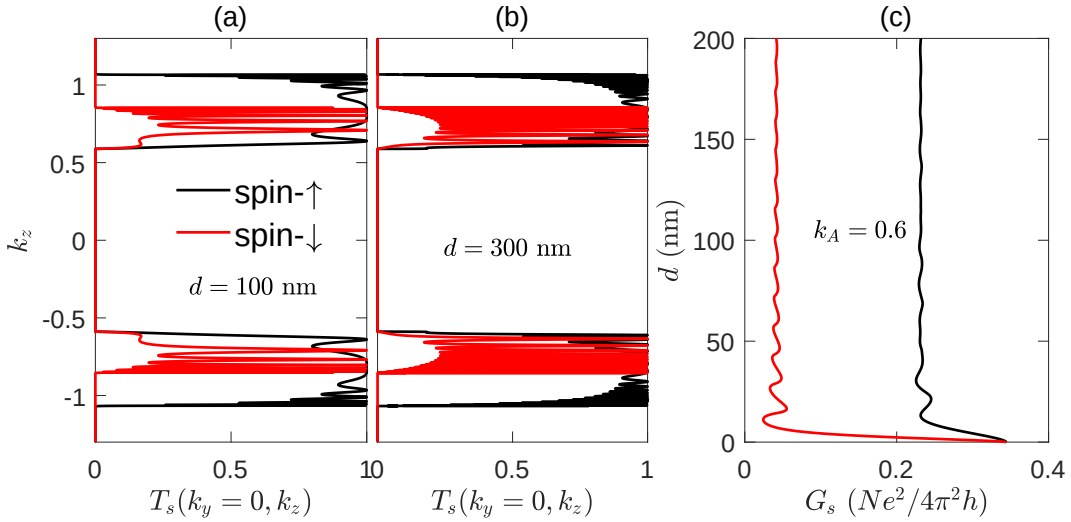

FIG. 1: (a)-(b) The spin-dependent transmission probability $T_s(k_y = 0, k_z)$ vs k_z for $k_A = 0.6$ nm^{-1}, with (a) $d = 100$ nm and (b) $d = 300$ nm. (c) The spin-dependent conductances as functions of the width d of the junction.

Inserting Eqs. (A5) and (A7) into

$$\mathcal{H}^s_{\rm eff}(\mathbf{k}) = \mathcal{H}^s_{0,0} + \frac{[\mathcal{H}^s_{1,0}, \mathcal{H}^s_{0,1}]}{\omega}, \tag{A8}$$

the effective Hamiltonian $\mathcal{H}_{\rm eff}(\mathbf{k}) = \mathcal{H}^+_{\rm eff}(\mathbf{k}) \oplus \mathcal{H}^-_{\rm eff}(\mathbf{k})$ finally takes the form as given by Eq. (3) of the main text.

Supplementary material B: Effect of d on the transmission probability and conductance

Our numerical calculations show that, while the pattern of $T_s(k_y, k_z)$ in the k_y-k_z plane changes with d, the conductance is insensitive to the width d of the junction when d is large enough. This can be understood as follows. With the transmission coefficient Eq. (9) in the main text, we can obtain the transmission probability as

$$T_s(k_y, k_z) = |t_s|^2 = \frac{4\mathcal{F}_1^2\mathcal{F}_2^2}{4\mathcal{F}_1^2\mathcal{F}_2^2 + \left[(\mathcal{F}_1^2 - \mathcal{F}_2^2)^2 + 2\Delta_y^2(\mathcal{F}_1^2 + \mathcal{F}_2^2) + \Delta_y^4\right]\sin^2(k_2 d)}, \tag{A9}$$

where k_2, being function of k_y and k_z, i.e.,

$$k_2 = \frac{1}{v_s}\sqrt{E^2 - |\tilde{M}(\mathbf{k}) - s\lambda|^2 - v_s^2(k_y + s\frac{v_1}{v_s}k_z\sin\phi)^2}, \tag{A10}$$

is spin dependent. As shown by Eq. (A9), for $k_2 = n\pi/d$, $T_s(k_y, k_z) = 1$ exhibits perfect transmission, which is attributed to the well-known Klein tunneling effect [7, 8].

From Eq. (A9), one can see that the transmission probability $T_s(k_y, k_z)$ depends on d only through the trigonometric function $\sin^2(k_2 d)$. Obviously, the increase of d would modify the oscillation period of $\sin^2(k_2 d)$ and thus affect $T_s(k_y, k_z)$ drastically, as shown in Fig. 3 of the main text. To see this more clearly, we plot $T_s(k_y = 0, k_z)$ as functions of k_z in Figs. 1(a) and (b). For d large enough, the increase of d only increases the number of the high-frequency oscillations in the overlap regions but does not change the average value of the transmission probability. Therefore, after integral over k_y and k_z, both conductances $G_\uparrow$ and $G_\downarrow$ almost remain a constant value. In order to verify this, we also plot the dependence of G_s on d in Fig. 1(c). Even though G_s oscillates for small d, the oscillations, for large d ($> 80nm$), become negligible and so the conductances almost remain a constant value.

Supplementary material C: Discussions about the role of an applied magnetic field/magnetic perturbation or a linearly polarized light

For a linearly polarized light, the vector potential for the light can be chosen as $\mathbf{A} = A_0\cos(\omega t)\mathbf{e}_1$, i.e., $\eta = 0$. In this case, both λ and $v_{1,2}$ vanish in Eq. (3) of the main text, so that the spin degeneracy always remains, seeing Eq. (4) in the main text.

Therefore, no WHM phase appears. If the system is subjected to an applied magnetic field/magnetic perturbation, the Weyl fermions is described by the Hamiltonian $H(\mathbf{k}) + \sum_{i=x,y,z} m_i \sigma_i \tau_0$. The magnetization along x/y direction will mix two spins and no spin polarization appears. For the magnetization along z direction $\mathbf{m} = m_z \hat{e}_z$, the quasienergy spectrum of the Hamiltonian is

$$\epsilon_{s,\pm}(\mathbf{k}) = \epsilon_0(\mathbf{k}) + s m_z \pm \sqrt{|M(\mathbf{k})|^2 + v_0^2(k_x^2 + k_y^2)}. \tag{A11}$$

From here, one can see that m_z only shifts the spectrums of $\epsilon_{\uparrow,\pm}(\mathbf{k})$ and $\epsilon_{\downarrow,\pm}(\mathbf{k})$ to opposite directions in energy, but cannot realize the creation and annihilation of the Weyl node pairs. Therefore, an applied magnetic field/magnetic perturbation or a linearly polarized light can not achieve the interesting WHM phase.

Supplementary material D: Model Realization

1. Floquet theory in lattice model

Considering the spatial dependence or spatial confinement of the light, we first derive for the effective lattice model Hamiltonian. For the minimal model in Eq. (1) of the main text, the mapping to a cuboid lattice is obtained by the substitutions $k_i \to \frac{1}{a_i}\sin(k_i a_i)$ and $k_i^2 \to \frac{2}{a_i^2}[1 - \cos(k_i a_i)]$. Performing the Fourier transformation, we obtain the following static tight-binding Hamiltonian

$$H_{\text{stat}} = \sum_i c_i^\dagger \epsilon_0 c_i + \sum_{ij} c_i^\dagger t_{ij} c_j + h.c., \tag{A12}$$

where $\epsilon_0 = \left(M_0 - \frac{2M_1}{a_\perp^2} - \frac{4M_2}{a_\parallel^2}\right)\sigma_z$ and

$$t_{ij} = \begin{pmatrix} \frac{M_2}{a_\parallel^2} & -is\frac{v_0}{2a_\parallel} \\ -is\frac{v_0}{2a_\parallel} & -\frac{M_2}{a_\parallel^2} \end{pmatrix}\delta_{i,j-\hat{x}a_\parallel} + \begin{pmatrix} \frac{M_2}{a_\parallel^2} & \frac{v_0}{2a_\parallel} \\ -\frac{v_0}{2a_\parallel} & -\frac{M_2}{a_\parallel^2} \end{pmatrix}\delta_{i,j-\hat{y}a_\parallel} + \begin{pmatrix} \frac{M_1}{a_\perp^2} & 0 \\ 0 & -\frac{M_1}{a_\perp^2} \end{pmatrix}\delta_{i,j-\hat{z}a_\perp} \tag{A13}$$

with $a_{x,y} = a_\parallel$ and $a_z = a_\perp$ being lattice constants in the x-y plane and along the z direction, respectively. The trivial term $\epsilon_0(\mathbf{k})$ is omitted for the sake of brevity. For the central region, where the fermions are driven by the CPL, the time-dependent tight-binding Hamiltonian $H(t)$ is obtained from H_{stat} by substituting $t_{ij} \to e^{iA_{ij}} t_{ij}$, where

$$A_{ij} = \frac{e}{\hbar}\int_{\mathbf{r}_j}^{\mathbf{r}_i} \mathbf{A}(\mathbf{r}, t) \cdot d\mathbf{l} \tag{A14}$$

is phase change of the hopping integral due to the CPL. Subsequently, we can derive

$$\begin{aligned} H^s(t) = \sum_i c_i^\dagger \epsilon_0 c_i &+ \sum_i \left[e^{i\zeta_x \cos(\omega t + \eta\alpha_x)} c_i^\dagger \begin{pmatrix} \frac{M_2}{a_\parallel^2} & -is\frac{v_0}{2a_\parallel} \\ -is\frac{v_0}{2a_\parallel} & -\frac{M_2}{a_\parallel^2} \end{pmatrix} c_{i+\hat{x}a_\parallel} + h.c. \right] \\ &+ \sum_i \left[e^{i\zeta_y \cos(\omega t - \eta\alpha_y)} c_i^\dagger \begin{pmatrix} \frac{M_2}{a_\parallel^2} & \frac{v_0}{2a_\parallel} \\ -\frac{v_0}{2a_\parallel} & -\frac{M_2}{a_\parallel^2} \end{pmatrix} c_{i+\hat{y}a_\parallel} + h.c. \right] \\ &+ \sum_i \left[e^{-i\zeta_z \cos\omega t} c_i^\dagger \begin{pmatrix} \frac{M_1}{a_\perp^2} & 0 \\ 0 & -\frac{M_1}{a_\perp^2} \end{pmatrix} c_{i+\hat{z}a_\perp} + h.c. \right], \end{aligned} \tag{A15}$$

where

$$\begin{aligned} \zeta_x &= k_A a_\parallel \sqrt{\cos^2\theta\cos^2\phi + \sin^2\phi} \\ \zeta_y &= k_A a_\parallel \sqrt{\cos^2\theta\sin^2\phi + \cos^2\phi} \\ \zeta_z &= k_A a_\perp \sin\theta \end{aligned} \tag{A16}$$

and

$$\begin{aligned} \sin\alpha_x &= \frac{\sin\phi}{\sqrt{\cos^2\theta\cos^2\phi + \sin^2\phi}} \\ \sin\alpha_y &= \frac{\cos\phi}{\sqrt{\cos^2\theta\sin^2\phi + \cos^2\phi}}. \end{aligned} \tag{A17}$$

Now, the spacial dependence of the vector potential can be taken into account, i.e.,

$$k_A = \frac{eA_0}{\hbar}\cos\left(\frac{2\pi}{\lambda_c}\mathbf{n}\cdot\mathbf{r}\right) = \frac{eA_0}{\hbar}\cos\left(2\pi\frac{x\sin\theta\cos\phi + y\sin\theta\sin\phi + z\cos\theta}{\lambda_c}\right) \tag{A18}$$

with λ_c the wavelength of the CPL. By using the relation

$$e^{ix\cos\xi} = \sum_{n=-\infty}^{\infty}(i)^n J_n(x)e^{in\xi} \tag{A19}$$

and performing the Fourier transformation on the basis and time, we can further derive the photodressed lattice Hamiltonian

$$\begin{aligned}
\mathcal{H}^s_{00} &= M'(\mathbf{k})\sigma_z + s\frac{J_{0,x}v_0}{a_\parallel}\sin(k_x a_\parallel)\sigma_x - \frac{J_{0,y}v_0}{a_\parallel}\sin(k_y a_\parallel)\sigma_y \\
\mathcal{H}^s_{1,0} &= M_{10}(\mathbf{k})\sigma_z + se^{-i\eta\alpha_x}\frac{J_{1,x}v_0}{a_\parallel}\cos(k_x a_\parallel)\sigma_x - e^{i\eta\alpha_y}\frac{J_{1,y}v_0}{a_\parallel}\cos(k_y a_\parallel)\sigma_y \\
\mathcal{H}^s_{0,1} &= M_{01}(\mathbf{k})\sigma_z + se^{i\eta\alpha_x}\frac{J_{1,x}v_0}{a_\parallel}\cos(k_x a_\parallel)\sigma_x - e^{-i\eta\alpha_y}\frac{J_{1,y}v_0}{a_\parallel}\cos(k_y a_\parallel)\sigma_y,
\end{aligned} \tag{A20}$$

where

$$\begin{aligned}
M'(\mathbf{k}) &= M_0 - \sum_i \frac{2M_i}{a_i^2} + \sum_i \frac{2J_{0,i}M_i}{a_i^2}\cos(k_i a_i) \\
M_{10}(\mathbf{k}) &= -e^{-i\eta\alpha_x}\frac{2J_{1,x}M_2}{a_\parallel^2}\sin(k_x a_\parallel) - e^{i\eta\alpha_y}\frac{2J_{1,y}M_2}{a_\parallel^2}\sin(k_y a_\parallel) + \frac{2J_{1,z}M_1}{a_\perp^2}\sin(k_z a_\perp) \\
M_{01}(\mathbf{k}) &= -e^{i\eta\alpha_x}\frac{2J_{1,x}M_2}{a_\parallel^2}\sin(k_x a_\parallel) - e^{-i\eta\alpha_y}\frac{2J_{1,y}M_2}{a_\parallel^2}\sin(k_y a_\parallel) + \frac{2J_{1,z}M_1}{a_\perp^2}\sin(k_z a_\perp)
\end{aligned} \tag{A21}$$

with $M_z = M_1$, $M_{x,y} = M_2$, $J_{n,i} = J_n(\zeta_i)$ and $J_n(x)$ the n-th order Bessel function. In the off-resonance regime, the Bessel functions $J_n(x)$ with $n > 1$ are negligible. Therefore, the effective lattice Hamiltonian for the driving region can be approximated as

$$\begin{aligned}
H^s_{\text{eff}} &= \mathcal{H}^s_{0,0} + \frac{[\mathcal{H}^s_{1,0}, \mathcal{H}^s_{0,1}]}{\omega} \\
&= \left[M'(\mathbf{k}) - s\eta\frac{2v_0^2}{a_\parallel^2}\frac{J_{1,x}J_{1,y}}{\omega}\sin(\alpha_x+\alpha_y)\cos(k_x a_\parallel)\cos(k_y a_\parallel)\right]\sigma_z \\
&+ \left[s\frac{J_{0,x}v_0}{a_\parallel} - \eta\frac{4M_2 v_0}{a_\parallel^3}\frac{J_{1,x}J_{1,y}}{\omega}\sin(\alpha_x+\alpha_y)\cos(k_y a_\parallel)\right]\sin(k_x a_\parallel)\sigma_x \\
&- \left[\frac{J_{0,y}v_0}{a_\parallel} - s\eta\frac{4M_2 v_0}{a_\parallel^3}\frac{J_{1,x}J_{1,y}}{\omega}\sin(\alpha_x+\alpha_y)\cos(k_x a_\parallel)\right]\sin(k_y a_\parallel)\sigma_y \\
&+ \eta\frac{4M_1 v_0}{a_\parallel a_\perp^2}\left[\frac{J_{1,y}J_{1,z}}{\omega}\sin\alpha_y\cos(k_y a_\parallel)\sigma_x - s\frac{J_{1,x}J_{1,z}}{\omega}\sin\alpha_x\cos(k_x a_\parallel)\sigma_y\right]\sin(k_z a_\perp).
\end{aligned} \tag{A22}$$

Subsequently, we obtain the following tight-binding Hamiltonian for the driving region

$$H^s_{\text{D}} = \sum_i c_i^\dagger \epsilon_0 c_i + \sum_{ij} c_i^\dagger\left(t_{1,ij} + t_{2,ij}\right)c_j + h.c., \tag{A23}$$

where

$$t_{1,ij} = J_{0,x}\begin{pmatrix} \frac{M_2}{a_\parallel^2} & -is\frac{v_0}{2a_\parallel} \\ -is\frac{v_0}{2a_\parallel} & -\frac{M_2}{a_\parallel^2}\end{pmatrix}\delta_{i,j-\hat{x}a_\parallel} + J_{0,y}\begin{pmatrix} \frac{M_2}{a_\parallel^2} & \frac{v_0}{2a_\parallel} \\ -\frac{v_0}{2a_\parallel} & -\frac{M_2}{a_\parallel^2}\end{pmatrix}\delta_{i,j-\hat{y}a_\parallel} + J_{0,z}\begin{pmatrix} \frac{M_1}{a_\perp^2} & 0 \\ 0 & -\frac{M_1}{a_\perp^2}\end{pmatrix}\delta_{i,j-\hat{z}a_\perp} \tag{A24}$$

and

$$\begin{aligned}
t_{2,ij} &= \left(iv_2\sigma_x - isv_2\sigma_y - s\lambda\sigma_z\right)\delta_{i,j-\hat{x}a_\parallel-\hat{y}a_\parallel} + \left(iv_2\sigma_x + isv_2\sigma_y - s\lambda\sigma_z\right)\delta_{i,j-\hat{x}a_\parallel+\hat{y}a_\parallel} \\
&+ isv_x\sigma_y\delta_{i,j-\hat{x}a_\parallel-\hat{z}a_\perp} - isv_x\sigma_y\delta_{i,j-\hat{x}a_\parallel+\hat{z}a_\perp} - iv_y\sigma_x\delta_{i,j-\hat{y}a_\parallel-\hat{z}a_\perp} + iv_y\sigma_x\delta_{i,j-\hat{y}a_\parallel+\hat{z}a_\perp}
\end{aligned} \tag{A25}$$

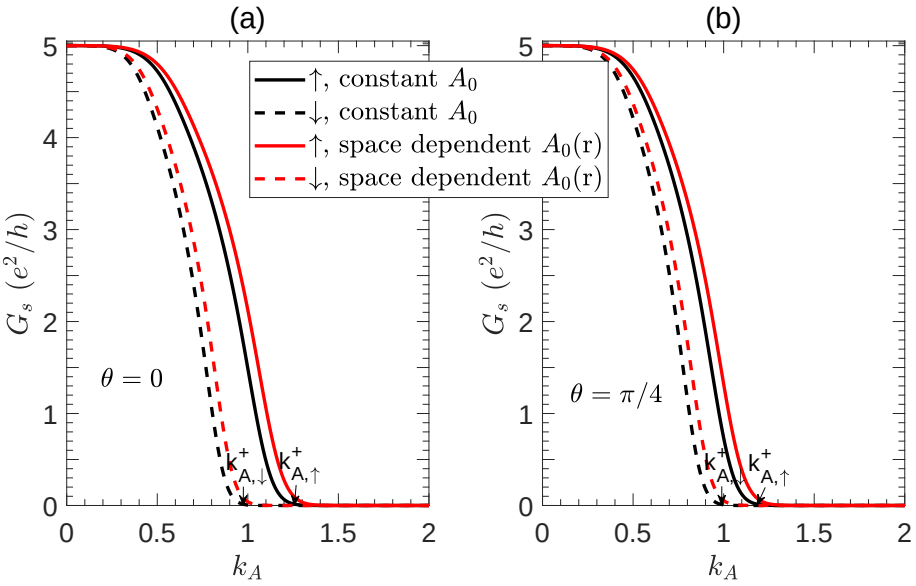

FIG. 2: Effect of spatially periodic dependence of the vector potential on the spin-dependent conductances G_s with $\phi = \pi/2$, and (a) $\theta = 0$ and (b) $\theta = \pi/4$. The lattice size of the junction is chosen as $20a_\parallel \times 20a_\parallel \times 20a_\perp$ with $a_\parallel = a_\perp = a$, and $\lambda_c = 90a$ for numerical calculations using KWANT[9].

with

$$\lambda = \frac{\eta v_0^2}{2a_\parallel^2}\frac{J_{1,x}J_{1,y}}{\omega}\sin(\alpha_x+\alpha_y)$$
$$v_2 = \frac{\eta M_2 v_0}{a_\parallel^3}\frac{J_{1,x}J_{1,y}}{\omega}\sin(\alpha_x+\alpha_y)$$
$$v_{x,y} = \frac{\eta M_1 v_0}{a_\parallel a_\perp^2}\frac{J_{1,x,y}J_{1,z}}{\omega}\sin\alpha_{x,y}. \tag{A26}$$

As shown by Eqs. (A23) and (A25), the off-resonant CPL, on one hand, modifies the nearest hopping integral and, on the other hand, introduces second nearest hopping to the lattice Hamiltonian.

2. Effect of spatially periodic dependence of the vector potential along propagation direction of the light

As we know, when light propagates along an incident direction, the vector potential is spatially periodic, which takes the form $\mathbf{A} = A_0(\mathbf{r})[\cos(\omega t)\mathbf{e}_1 - \eta\sin(\omega t)\mathbf{e}_2]$, where

$$A_0(\mathbf{r}) = A_0\cos\left(\frac{2\pi}{\lambda_c}\mathbf{n}\cdot\mathbf{r}\right) = A_0\cos\left(2\pi\frac{x\sin\theta\cos\phi + y\sin\theta\sin\phi + z\cos\theta}{\lambda_c}\right) \tag{A27}$$

with $\mathbf{e}_{1,2}$ being two unit vectors perpendicular to the incident direction $\mathbf{n}$. When taking into account the spacial inhomogeneity of the vector potential, the photodressed lattice Hamiltonian is given by Eq. (A23). Obviously, the problems are unable to be solved analytically. In this discussion, we employ the widely adopted transport package KWANT[9], which is convenient to deal with this problem numerically. For specifical calculations, the size of the sample is taken to be $20a_\parallel \times 20a_\parallel \times 20a_\perp$ with $a_\parallel = a_\perp = a$, and the calculated results for spin-resolved conductances G_s are plotted in Fig. 2. Compared the results with (red lines) and without (black lines) the spacial inhomogeneity, one can find that the spacial inhomogeneity due to propagation of the light only shifts the critical values of k_A, but does not change the spin filter effect qualitatively, whether for vertical ($\theta = 0$) or oblique ($\theta = \pi/4$) incidence. This influence can be greatly reduced if keeping $x, y, z \ll \lambda_c$.

Experimentally, the sample can be fabricated as a microribbon as illustrated in Fig. 1(b) of the main text, with several hundreds of nanometer in width (y direction) and thickness (z direction), and several micrometers in length (x direction). Since the thickness and width of the sample are much smaller than the wavelength of the light, the spatial inhomogeneity of the vector potential along y and z directions can be ignored safely. At the same time, if choosing the incident direction $\mathbf{n}$ with $\phi = \frac{\pi}{2}$ (i.e., tilting in the y-z plane), or confining the irradiation region d in several hundreds of nanometer, the spatially periodic dependence of the vector potential along the junction (x direction) also can be negligible. On the other hand, although the size of several

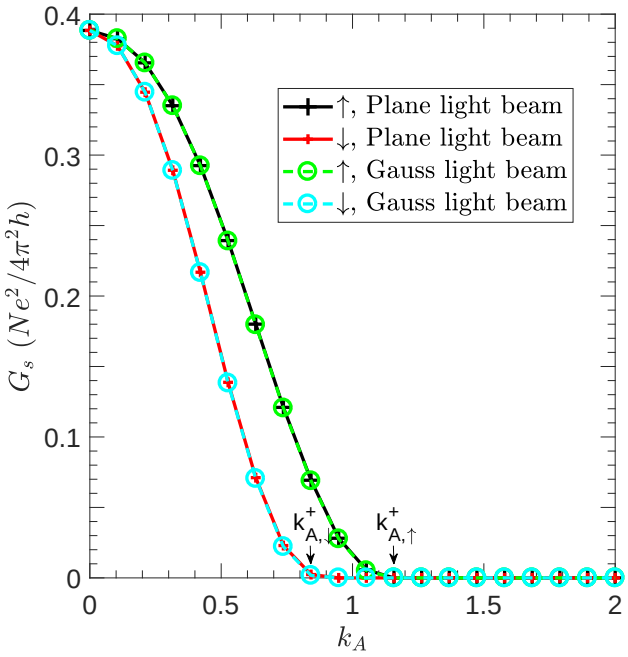

FIG. 3: Conductances with the incident plane light beam and the Gauss light beam irradiating from vertical direction $\theta = 0$. The Gauss distribution of the light intensity takes the form of $A_0 \to A_0(\mathbf{r}) = \frac{A_0}{D} exp[\frac{-(x^2+y^2)}{D^2}]$, where we set the spot radius $D = d/2$ locating at the boundaries between the irradiation region and reservoirs. The length of the irradiation region is set as $d = 500a$ for numerical calculations using KWANT[9].

hundreds of nanometer is far smaller than the wavelength of the light, it is greatly larger than the Bloch wavelength of the electrons. Thus, the numerical results calculated with the lattice model, i.e., above Fig. 2, are qualitatively consistent with the analytical results calculated with the continuous model, i.e., Fig. 4 in the main text. In experiments, one should irradiate the light along z ($\theta = 0$), where the spin filter effect is strongest and the influence of the spatial inhomogeneity is weakest.

3. Realization of the model with light confinement

In the model of Fig. 1(b) in the main text, we assume that the light intensity is uniform inside the junction and drops to zero outside. Experimentally, to confine the light in the width of d and to reach the most prominent spin filter effect, one can irradiate a beam of gaussian-profile light along z direction ($\theta = 0$). In this situation, the vector potential A_0 in Eq. (2) of the main text is modified to $A_0 \to A_0(\mathbf{r}) = \frac{A_0}{D} exp[\frac{-(x^2+y^2)}{D^2}]$, where we set the spot radius $D = d/2$ locating at the boundaries between the irradiation region and reservoirs.

Including the spatial dependence of the light intensity, we perform numerical calculations with the lattice model. For simplicity, we neglect spatially periodic dependence of the vector potential along propagation direction z. Taking k_y and k_z as parameters, we map the continuous Hamiltonian to a one-dimensional chain along direction x and then perform numerical calculations using KWANT. The numerical results are presented in Fig. 3. As seen from Fig. 3, the conductances calculated with the gaussian-profile light beam (with $A_0(\mathbf{r})$) exhibit almost the same spin filter effect as that calculated with the plane light beam (constant A_0). This, in fact, can be expected, since the Gauss distribution of the light intensity is mainly to renormalize the effective width of the junction, while as discussed in supplementary material B, the conductances are independent on the width of the junction for the chosen light beam. These numerical results are also consistent with the analytical calculations in the main text.

4. Realization of the model without light confinement

In fact, we can loose the restriction of focusing the light on the central region for the model in Fig. 1(b) of the main text. Alternatively, in this setup, one can replace two Weyl-semimetal reservoirs with two normal-metal electrodes, i.e., fabricating a normal metal/Weyl semimetal/normal metal junction. The light can irradiate on the whole system. In order to reach the strongest spin filter effect, one should irradiate the light along z ($\theta = 0$). Due to trivial response of the normal-metal electrodes to the irradiation, the transport is determined by the WHM phase.

For this normal metal/Weyl semimetal/normal metal junction, the effective tight-binding Hamiltonian for the middle region is given by Eq. (A23) and the continuous Hamiltonian for the normal metal leads is $H_{lead} = \frac{\hbar^2 k^2}{2m} - \mu$, with m the mass and μ

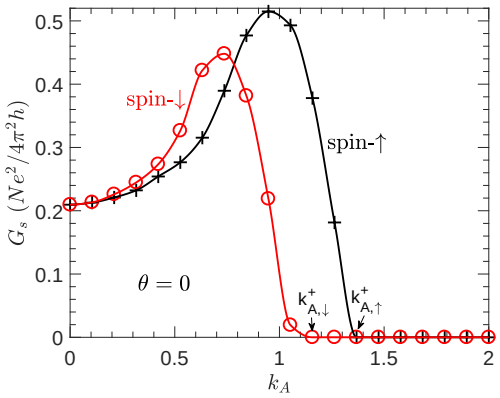

FIG. 4: Spin-dependent conductances in a normal metal/Weyl semimetal/normal metal junction as functions of the CPL intensity k_A, with $\theta = 0$, $t = 0.1$ eV, and $\mu = 0.1$ eV. Other parameters chosen the same as Fig. 3.

the chemical potential. Following the procedure in piont 1 of supplementary material D, we first obtain the static tight-binding Hamiltonian for the normal metal leads as

$$H_{lat} = \sum_i (-\mu + 6t)\, c_i^\dagger c_i - \left(t \sum_{\langle ij \rangle} c_i^\dagger c_j + h.c. \right) \tag{A28}$$

with $t = \frac{\hbar^2}{2ma^2}$ the nearest neighbouring hopping integral and a the lattice constant. In the presence of the CPL, the effective lattice Hamiltonian for the normal metal leads can be derived as

$$H_{lat}^{\text{eff}} = \sum_i (-\mu + 6t)\, c_i^\dagger c_i - t \sum_i \left(J_{0,x} c_i^\dagger c_{i+\hat{x}a} + J_{0,y} c_i^\dagger c_{i+\hat{y}a} + J_{0,z} c_i^\dagger c_{i+\hat{z}a} + h.c. \right), \tag{A29}$$

from which we can see that the response of the normal metal leads to the CPL is quite trivial, namely, although the nearest neighboring hopping integral t is renormalized, no additional hopping terms are introduced.

Performing the Fourier transform on Eqs. (A23) along the y and z directions and ignoring the spatial dependence of CPL, we can approximate

$$H_{\text{D}}^s = \sum_{i \in x_m/a} \left[c_i^\dagger \epsilon_0' c_i + \left(c_i^\dagger t_m c_{i+1} + h.c. \right) \right], \tag{A30}$$

in the vicinity of the gap closing points for the middle region $x_m \in [0, d]$, with

$$\begin{aligned} \epsilon_0' = {} & 4v_y \sin(k_z a)\sigma_x - \left[\left(\frac{J_{0,y} v_0}{a} - 4sv_2 \right) \sin(k_y a) + 4sv_x \sin(k_z a) \right] \sigma_y \\ & + \left[M_0 - \frac{2M_1}{a^2} - \frac{4M_2}{a^2} + \frac{2J_{0,y} M_2}{a^2} \cos(k_y a) + \frac{2J_{0,z} M_2}{a^2} \cos(k_z a) - 4s\lambda \right] \sigma_z, \end{aligned} \tag{A31}$$

and

$$t_m = \frac{J_{0,x} M_2}{a^2} \sigma_z - \frac{i}{2} \left(s \frac{J_{0,x} v_0}{a} - 4v_2 \right) \sigma_x. \tag{A32}$$

Similarly, for the normal metal leads with $x_L \in (-\infty, -a] \cup [d + a, +\infty)$, we can derive the one-dimensional lattice Hamiltonian as

$$H_{lat}^{\text{eff}} = \sum_{i \in x_L/a} \left[-\mu + 6t - 2tJ_{0,y} \cos(k_y a) - 2tJ_{0,z} \cos(k_z a) \right] c_i^\dagger c_i - t \sum_{i \in x_L/a} \left(J_{0,x} c_i^\dagger c_{i+1} + h.c. \right). \tag{A33}$$

The coupling Hamiltonian between the middle region and two normal-metal leads can be obtained via the last term of Eq. (A33) by fixing $i = -1$ and d/a.

We carry out the numerical calculations using KWANT and the numerical results are presented in Fig. 4. As expected, figure 4 shows the prominent spin filter effect. Compared with the Weyl-semimetal electrodes, the difference here is that there is a drop below the spin filter region. It is easy to be understood. Without the CPL, the Fermi surface of Weyl-semimetal electrodes is completely overlapped with one in the middle region, and so the conductance is largest. In contrast, the Fermi surface of the normal-metal electrodes is located in the middle of two Weyl nodes, in which the overlapping area between the middle region and the electrodes is small. With increase of the illumination, the reduced distance between two Weyl nodes makes the overlapping area first increase and then decrease due to open of the energy gap band, which leads to nonmonotonical behavior in Fig. 4. In this process, the effect of the CPL on the normal metal mainly renormalizes its chemical potential, namely, changing the rate of descent below the spin-filter region but never changes $k^{+}_{A,\sigma}$ because it is determined by phase boundary of the WSM phase. In fact, the spin filter effect as a spin-related transport, originating from the spin-polarized band in WHM phase, is quite insensitive to the nonmagnetic electrodes and junction details.

Supplementary material E: Kwant scripts related to the numerical simulations

In this section, we would attach the Kwant scripts related to the numerical simulations in supplemental material D as follows.

1. Effect of spatially periodic dependence of the vector potential

```
#!/usr/bin/env python3
# -*- coding: utf-8 -*-
"""
@author: Ming-Xun Deng
"""
import kwant

from matplotlib import pyplot

from scipy import special

import numpy as np

import tinyarray

# define Pauli-matrices for convenience
sigma_0 = tinyarray.array([[1, 0], [0, 1]])

sigma_x = tinyarray.array([[0, 1], [1, 0]])

sigma_y = tinyarray.array([[0, -1j], [1j, 0]])

sigma_z = tinyarray.array([[1, 0], [0, -1]])

# system parameters

a = 1

yita = 1

theta = 0

phi = np.pi / 2

omega = 1

Ef = 0.01

v0 = 0.24598
```

```
M0 = - 0.08686

M1 = - 0.106424

M2 = - 0.103610

L_c = 100  #  light wavelength

Gauss = 0  # 0 plane beam and > 0 for Gaussian light beam

L = 20

W = 20

H = 20

rho_x = np.sqrt( np.cos(theta)**2 * np.cos(phi)**2 + np.sin(phi)**2 )

rho_y = np.sqrt( np.cos(theta)**2 * np.sin(phi)**2 + np.cos(phi)**2 )

rho_z = np.sin(theta)

sin_ax = np.sin(phi) / rho_x

sin_ay = np.cos(phi) / rho_y

sin_xy = ( np.sin(phi) * np.cos(theta) * np.sin(phi) \
        + np.cos(theta) * np.cos(phi) * np.cos(phi) )/(rho_x * rho_y )

def make_system( s = 1, A0 = 0 ):
    # Start with an empty tight-binding system and a single square lattice.
    # ‘a‘ is the lattice constant (by default set to 1 for simplicity).

    lat = kwant.lattice.cubic( a )

    sys = kwant.Builder( )

    def hopping( h_type ):

        def hop_phi( sitei, sitej ):

            ( xi, yi, zi ) = sitei.pos

            ( xj, yj, zj ) = sitej.pos

            x = ( xi + xj ) / 2

            y = ( yi + yj ) / 2

            z = ( zi + zj ) / 2

            r_n = ( x - L / 2 )*np.sin(theta)*np.cos(phi) \
                 + ( y - W / 2 )*np.sin(theta)*np.sin(phi) + ( z- H /2 ) * np.cos(theta)

            R_G = ( x - L / 2 ) ** 2 + ( y - W / 2 ) ** 2 + ( z- H /2 ) **2 - r_n ** 2
```

```
        if np.abs(Gauss) > 0:
            pA =  np.exp( - R_G / Gauss ** 2  )
        else:
            pA = 1

        if np.abs( L_c ) > 0:
            kA = pA * A0 * np.cos( 2*np.pi * r_n / L_c  )
        else:
            kA = pA * A0

        J_0x = special.jv(0, kA * rho_x )

        J_0y = special.jv(0, kA * rho_y )

        J_0z = special.jv(0, kA * rho_z )

        J_1x = special.jv(1, kA * rho_x )

        J_1y = special.jv(1, kA * rho_y )

        J_1z = special.jv(1, kA * rho_z )

        v2 = yita * M2 * v0 * J_1x * J_1y * sin_xy / omega

        vx = yita * M1 * v0 * J_1x * J_1z * sin_ax / omega

        vy = yita * M1 * v0 * J_1y * J_1z * sin_ay / omega
        lam = yita * v0 **2 * J_1x * J_1y * sin_xy / ( 2 * omega )

        if h_type == 1 :
            return J_0x * ( M2 * sigma_z - s * 1j * v0 / 2 * sigma_x )
        elif h_type == 2 :
            return J_0y * ( M2 * sigma_z + 1j * v0 / 2 * sigma_y )
        elif h_type == 3:
            return J_0z * M1 * sigma_z
        elif h_type == 4:
            return 1j * v2 * sigma_x - 1j * s * v2 * sigma_y - s * lam * sigma_z
        elif h_type == 5:
            return 1j * v2 * sigma_x + 1j * s * v2 * sigma_y - s * lam * sigma_z
        elif h_type == 6:
            return 1j * s * vx * sigma_y
        elif h_type == 7:
            return - 1j * s * vx * sigma_y
        elif h_type == 8:
            return - 1j * vy * sigma_x
        else:
            return 1j * vy * sigma_x

    hopping_coeff = hop_phi

    return hopping_coeff

#### Define the scattering region. ####
sys[( lat(i, j, k) for i in range(L) for j in range(W) for k in range(H) )] = \
    ( M0 - 2 * M1 - 4 * M2 ) * sigma_z
```

```
    # hoppings in x-direction
    sys[kwant.builder.HoppingKind((1, 0, 0), lat, lat)] = hopping( 1 )
    # hoppings in y-directions
    sys[kwant.builder.HoppingKind((0, 1, 0), lat, lat)] = hopping( 2 )
    # hoppings in z-directions
    sys[kwant.builder.HoppingKind((0, 0, 1), lat, lat)] = hopping( 3 )

    ## second nearest hopping
    sys[kwant.builder.HoppingKind((1,  1,  0), lat, lat)] = hopping( 4 )
    sys[kwant.builder.HoppingKind((1, -1,  0), lat, lat)] = hopping( 5 )
    sys[kwant.builder.HoppingKind((1,  0,  1), lat, lat)] = hopping( 6 )
    sys[kwant.builder.HoppingKind((1,  0, -1), lat, lat)] = hopping( 7 )
    sys[kwant.builder.HoppingKind((0,  1,  1), lat, lat)] = hopping( 8 )
    sys[kwant.builder.HoppingKind((0,  1, -1), lat, lat)] = hopping( 9 )
    #### Define the left lead. ####
    lead = kwant.Builder(kwant.TranslationalSymmetry((-a, 0,0)))
    lead[( lat(0, j, k ) for j in range(W) for k in range(H) )] = \
        ( M0 - 2 * M1 - 4 * M2 ) * sigma_z
    # hoppings in x-direction
    lead[kwant.builder.HoppingKind((1, 0, 0), lat, lat)] = \
        M2 * sigma_z - s * 1j * v0 / 2 * sigma_x
    # hoppings in y-directions
    lead[kwant.builder.HoppingKind((0, 1, 0), lat, lat)] = \
        M2 * sigma_z + 1j * v0 / 2 * sigma_y
    # hoppings in z-directions
    lead[kwant.builder.HoppingKind((0, 0, 1), lat, lat)] = \
        M1 * sigma_z

    #### Attach the leads and return the finalized system. ####
    sys.attach_lead(lead)
    sys.attach_lead(lead.reversed())

    return sys

def plot_conductance(Ax):
    # Compute conductance

    data1 = []
    data2 = []

    for A0 in Ax:

        s =  1

        sys = make_system( s, A0  )

        sys = sys.finalized()

        smatrix = kwant.smatrix(sys, energy = Ef)

        data1.append( smatrix.transmission(1, 0) )

        s =  -1

        sys = make_system( s, A0  )
```

```
        sys = sys.finalized()

        smatrix = kwant.smatrix(sys, energy = Ef)

        data2.append(smatrix.transmission(1, 0) )

        print( A0 )

    pyplot.figure()
    pyplot.plot(Ax, data1,'k-', Ax, data2,'r--')
    pyplot.xlabel("kA")
    pyplot.ylabel("conductance [e^2/h]")
    pyplot.show()

    return data1, data2

def main():

    syst = make_system( )

    # Check that the system looks as intended.
    kwant.plot(syst)

    # Finalize the system.
    syst = syst.finalized()

    plot_conductance( Ax = np.linspace( 0.0, 2, 200) )

# Call the main function if the script gets executed (as opposed to imported).
# See <http://docs.python.org/library/__main__.html>.
if __name__ == '__main__':
    main()
```

2. Realization of the model with light confinement

```
#!/usr/bin/env python3
# -*- coding: utf-8 -*-
"""
@author: Ming-Xun Deng
"""
import kwant

import numpy as np

import tinyarray

from matplotlib import pyplot

from scipy import special

# define the pauli matrix

sigma_0=tinyarray.array([[1,0],[0,1]])

sigma_x=tinyarray.array([[0,1],[1,0]])
```

```
sigma_y=tinyarray.array([[0,-1j],[1j,0]])

sigma_z=tinyarray.array([[1,0],[0,-1]])

## system parameters

a = 1

yita = 1

theta = 0

phi = np.pi / 2

omega = 1

Ef = 0.05

v0 = 0.24598

M0 = - 0.08686

M1 = - 0.106424

M2 = - 0.103610

Lx = 500

Gauss = 0 #  0 for plane beam and > 0 for Gaussian light beam

rho_x = np.sqrt( np.cos(theta)**2 * np.cos(phi)**2 + np.sin(phi)**2 )

rho_y = np.sqrt( np.cos(theta)**2 * np.sin(phi)**2 + np.cos(phi)**2 )

rho_z = np.sin(theta)

sin_ax = np.sin(phi) / rho_x

sin_ay = np.cos(phi) / rho_y

sin_xy = np.cos(theta) / ( rho_x * rho_y )

def make_system( s=1, A0=0, ky=0, kz=0 ):

    lat = kwant.lattice.chain( a )

    sys = kwant.Builder( )

    for x in range( Lx ):

        if Gauss > 0:

            kA = A0 * np.exp( - ( x - Lx / 2 ) * 2 / Gauss ** 2 )
        else:
            kA = A0
```

```
        J_0x = special.jv(0, kA * rho_x )

        J_0y = special.jv(0, kA * rho_y )

        J_0z = special.jv(0, kA * rho_z )

        J_1x = special.jv(1, kA * rho_x )

        J_1y = special.jv(1, kA * rho_y )

        J_1z = special.jv(1, kA * rho_z )

        lam = yita * 2 * v0 ** 2 * J_1x * J_1y * sin_xy  / omega

        v1_x = yita * 4 * M1 * v0 * J_1x * J_1z * sin_ax  / omega

        v1_y = yita * 4 * M1 * v0  * J_1y * J_1z * sin_ay / omega

        v2 = yita * 4 * M2 * v0 * J_1x * J_1y * sin_xy  / omega

        ux = v1_y * np.sin( kz * a ) * sigma_x

        uy = ( (J_0y * v0 - s * v1_x) * np.sin( ky * a )  \
            + s * v1_x * np.sin( kz * a ) ) * sigma_y

        uz = ( M0 - 2 * M1 - 4 * M2 + 2 * J_0y * M2 * np.cos( ky * a ) \
            + 2 * J_0z * M1 * np.cos( kz * a )  - s * lam ) * sigma_z

        sys[ lat(x) ] = ux + uy + uz

        if x > 0 :
            sys[ lat(x-1), lat(x) ] = J_0x * M2 * sigma_z  \
                - 1j / 2 * ( s * J_0x * v0 - v2 ) * sigma_x


    sym_lead = kwant.TranslationalSymmetry([-a])

    lead = kwant.builder.Builder(sym_lead)

    hy = v0 * np.sin( ky * a ) * sigma_y

    hz = ( M0 - 2 * M1 - 4 * M2 + 2 * M2 * np.cos( ky * a )  \
        + 2 * M1 * np.cos( kz * a )  ) * sigma_z

    lead[ lat(0) ] = hy + hz

    lead[ lat(-1),lat(0) ]= M2 * sigma_z - 1j / 2 * s * v0 * sigma_x

    sys.attach_lead(lead)
    sys.attach_lead(lead.reversed())

    return sys

def plot_conductance(Ax, ksy, ksz ):

    data1 = []
```

```
    data2 = []

    for A0 in Ax:

        # Compute conductance
        spin_up = np.zeros( ( ksz.shape[0], ksz.shape[0] ) )

        spin_dw = np.zeros( ( ksz.shape[0], ksz.shape[0] ) )

        for m in range( len(ksz) ):

            kz = ksz[m]

            for n in range( len( ksy ) ):

                ky = ksy[n]

                s =  1

                sys = make_system( s, A0, ky, kz )

                sys = sys.finalized()

                smatrix = kwant.smatrix(sys, energy = Ef)

                spin_up[ m, n ] = smatrix.transmission(1, 0)

                s =  -1

                sys = make_system( s, A0, ky, kz )

                sys = sys.finalized()

                smatrix = kwant.smatrix(sys, energy = Ef)

                spin_dw[ m, n ] = smatrix.transmission(1, 0)

            print( kz )

        data1.append( spin_up.sum(0).sum(0) * ( ksz[1]-ksz[0] )*( ksy[1]-ksy[0] ) )

        data2.append( spin_dw.sum(0).sum(0) * ( ksz[1]-ksz[0] )*( ksy[1]-ksy[0] ) )
    pyplot.figure()
    pyplot.plot(Ax, data1,'k-', Ax, data2,'r-')
    pyplot.xlabel("kz")
    pyplot.ylabel("conductance [N/4pi^2 * e^2/h]")
    pyplot.show()

    return spin_up, spin_dw

def main():

    sys = make_system( )

    # Check that the system looks as intended.
```

```
    kwant.plot(sys)
    plot_conductance( Ax = np.linspace( 0, 2, 50 ), ksy = \
        np.linspace( -0.3, 0.3, 500 ), ksz = np.linspace( -1.3, 1.3, 500 ) )

# Call the main function if the script gets executed (as opposed to imported).
# See <http://docs.python.org/library/__main__.html>.
if __name__ == '__main__':
    main()
```

3. Realization of the model without light confinement

```
#!/usr/bin/env python3
# -*- coding: utf-8 -*-
"""
@author: Ming-Xun Deng
"""
import kwant

import numpy as np

import tinyarray

from matplotlib import pyplot

from scipy import special

# define the pauli matrix

sigma_0=tinyarray.array([[1,0],[0,1]])

sigma_x=tinyarray.array([[0,1],[1,0]])

sigma_y=tinyarray.array([[0,-1j],[1j,0]])

sigma_z=tinyarray.array([[1,0],[0,-1]])

## system parameters

a = 1

t = 0.1

mu = 0.2

yita = 1

theta = 0

phi = np.pi / 2

omega = 1

Ef = 0.05

v0 = 0.24598
```

```
M0 = - 0.08686

M1 = - 0.106424

M2 = - 0.103610

Lx = 500

Gauss = 0  # 0 plane beam and > 0 for Gaussian light beam

rho_x = np.sqrt( np.cos(theta)**2 * np.cos(phi)**2 + np.sin(phi)**2 )

rho_y = np.sqrt( np.cos(theta)**2 * np.sin(phi)**2 + np.cos(phi)**2 )

rho_z = np.sin(theta)

sin_ax = np.sin(phi) / rho_x

sin_ay = np.cos(phi) / rho_y

sin_xy = np.cos(theta) / ( rho_x * rho_y )

def make_system( s=1, A0=0, ky=0, kz=0 ):

    lat = kwant.lattice.chain( a )

    sys = kwant.Builder( )

    for x in range( Lx ):

        if Gauss > 0:

            kA = A0 * np.exp( - ( x - Lx / 2 ) * 2 / Gauss ** 2 )
        else:
            kA = A0

        J_0x = special.jv(0, kA * rho_x )

        J_0y = special.jv(0, kA * rho_y )

        J_0z = special.jv(0, kA * rho_z )

        J_1x = special.jv(1, kA * rho_x )

        J_1y = special.jv(1, kA * rho_y )

        J_1z = special.jv(1, kA * rho_z )

        lam = yita * 2 * v0 ** 2 * J_1x * J_1y * sin_xy  / omega

        v1_x = yita * 4 * M1 * v0 * J_1x * J_1z * sin_ax  / omega

        v1_y = yita * 4 * M1 * v0  * J_1y * J_1z * sin_ay / omega

        v2 = yita * 4 * M2 * v0 * J_1x * J_1y * sin_xy  / omega
```

```
        ux = v1_y * np.sin( kz * a ) * sigma_x

        uy = ( (J_0y * v0 - s * v1_x) * np.sin( ky * a )  \
            + s * v1_x * np.sin( kz * a ) ) * sigma_y

        uz = ( M0 - 2 * M1 - 4 * M2 + 2 * J_0y * M2 * np.cos( ky * a ) \
            + 2 * J_0z * M1 * np.cos( kz * a )  - s * lam ) * sigma_z

        sys[ lat(x) ] = ux + uy + uz

        if x > 0 :
            sys[ lat(x-1), lat(x) ] = J_0x * M2 * sigma_z  \
                - 1j / 2 * ( s * J_0x * v0 - v2 ) * sigma_x

    sym_lead = kwant.TranslationalSymmetry([-a])

    lead = kwant.builder.Builder(sym_lead)

    lead[ lat(0) ] = ( - mu + 6 * t - 2 * t * J_0y * np.cos( ky * a ) \
        - 2 * t * J_0z * np.cos( kz * a ) ) * sigma_0

    lead[ lat(-1), lat(0) ] = - t * J_0y * sigma_0

    sys.attach_lead(lead)
    sys.attach_lead( lead.reversed() )

    return sys

def plot_conductance(Ax, ksy, ksz ):

    data1 = []

    data2 = []

    for A0 in Ax:

        print( A0 )

        # Compute conductance
        spin_up = np.zeros( ( ksz.shape[0], ksz.shape[0] ) )

        spin_dw = np.zeros( ( ksz.shape[0], ksz.shape[0] ) )

        for m in range( len(ksz) ):

            kz = ksz[m]

            for n in range( len( ksy ) ):

                ky = ksy[n]

                s =  1

                sys = make_system( s, A0, ky, kz )

                sys = sys.finalized()
```

```
                smatrix = kwant.smatrix(sys, energy = Ef)

                spin_up[ m, n ] = smatrix.transmission(1, 0)

                s =  -1

                sys = make_system( s, A0, ky, kz )

                sys = sys.finalized()

                smatrix = kwant.smatrix(sys, energy = Ef)

                spin_dw[ m, n ] = smatrix.transmission(1, 0)

            print( kz )

        data1.append( spin_up.sum(0).sum(0) * ( ksz[1]-ksz[0] )*( ksy[1]-ksy[0] ) )

        data2.append( spin_dw.sum(0).sum(0) * ( ksz[1]-ksz[0] )*( ksy[1]-ksy[0] ) )

    pyplot.figure()
    pyplot.plot(Ax, data1,'k-', Ax, data2,'r-')
    pyplot.xlabel("kA")
    pyplot.ylabel("conductance [N/4pi^2 *e^2/h]")
    pyplot.show()

    return spin_up, spin_dw

def main():

    sys = make_system( )

    # Check that the system looks as intended.
    kwant.plot(sys)
    plot_conductance( Ax = np.linspace( 0, 2, 50 ), ksy = \
        np.linspace( -0.3, 0.3, 500 ), ksz = np.linspace( -1.3, 1.3, 500 ) )

# Call the main function if the script gets executed (as opposed to imported).
# See <http://docs.python.org/library/__main__.html>.
if __name__ == '__main__':
    main()
```


[1] M. S. Rudner, N. H. Lindner, E. Berg, and M. Levin, Phys. Rev. X **3**, 031005 (2013).
[2] P. Titum, N. H. Lindner, M. C. Rechtsman, and G. Refael, Phys. Rev. Lett. **114**, 056801 (2015).
[3] A. Farrell and T. Pereg-Barnea, Phys. Rev. Lett. **115**, 106403 (2015).
[4] C.-K. Chan, P. A. Lee, K. S. Burch, J. H. Han, and Y. Ran, Phys. Rev. Lett. **116**, 026805 (2016).
[5] Z. Yan and Z. Wang, Phys. Rev. Lett. **117**, 087402 (2016).
[6] M.-X. Deng, W. Y. Deng, D. X. Shao, R.-Q. Wang, R. Shen, L. Sheng, and D. Y. Xing, Phys. Rev. B **95**, 115102 (2017).
[7] N. Stander, B. Huard, and D. Goldhaber-Gordon, Phys. Rev. Lett. **102**, 026807 (2009).
[8] A. F. Young and P. Kim, Nat. Phys. **5**, 222 (2009).
[9] C. W. Groth, M. Wimmer, A. R. Akhmerov, X. Waintal, New J. Phys. **16**, 063065 (2014).